7

The Anisotropic Growth of Perovskite Oxide Nanowires

Yongming Hu, Haoshuang Gu and Zhao Wang
Faculty of Physics and Electronic Technology, Hubei University Wuhan, P R China

1. Introduction

A perovskite is any material with share the same type of crystal structure as calcium titanium oxide (i.e., a structure analogous to that of the natural crystal calcium titanate, known as the "perovskite structure"), yet exhibit a broad range of interesting and excellent physical and chemical properties, which have large and potential applications in solid fuel cell, solid electrolyte, sensor, solid resistor etc for its stablized crystal structure (Bhalla et al., 2000). Their structural properties, such as phase, crystallinity and dimensional play important roles for their fundamental performances, such as optical, electric-transport, phonon vibration and ferroelectric etc. With the size of ferroelectrics decreasing, the size-dependent ferroelectric behaviors and their possible disappearance at critical size become crucial. When synthesized of ferroelectric nanomaterials via a conventional solution process, perovskite materials with cubic or pseudo-cubic symmetry of its crystal structure tends to grow uniformly along three major directions, leading to the formation of nanopowders rather than a 1D structure (Wei et al., 2007 and Lu et al., 2002).

To realize an anisotropic growth, especially no surfactant used in the hydrothermal environment, the symmetry of crystal structrue has a crucial part for the anisotropic growth of nanowires (NWs), which is very interesting for technological application in nanodevice. In the last several years, long ferroelectric NWs with perovskite structures and anistropic growth have been synthesized by different solution approach. For example, Urban *et al*. realized the creation of well-isolated NWs [001] of $BaTiO_3$ using solution-phase decomposition of bimetallic alkoxide precursors and reported its ferroelectric switching, this allows for the RT tetragonal ferroelectric phase to possess polarization along the axis of the nanowire, and recently observed the ferroelectric phase transition in a single wire of $BaTiO_3$ (Urban et al., 2002 and Spanier et al., 2006). Xu *et al.* reported the anistropic growth of tetragonal perovskite $Pb(Zr_{0.52}Ti_{0.48})O_3$ (PZT) monocrystalline NWs [001] synthesized by polymer assisted hydrothermal method, showing that PZT nanorods were formed when assisted only by PVA, and PZT NWs were obtained when assisted by both PVA and PAA (Xu et al., 2005). Magrez *et al*. have realized the growth of highly uniform $KNbO_3$ NWs [011] exhibiting a narrow diameter distribution about 60 nm, the influence of the composition of the starting mixture as well as of the temperature-pressure within the hydrothermal autoclave on the product

purity and particle shape have also been identified (Magrez et al., 2006). Wang et al. reported the composite hydroxide mediated approach for the synthesis of nanostructures of complex functional oxides, including $BaTiO_3$, $BaMnO_3$, $BaCeO_3$ etc (Liu et al., 2006). In recent years, Rørvik *et al*. realized the anistropic growth of $PbTiO_3$ nanorod arrays on $SrTiO_3$ substrate with different orientation grown by self-assembly of nanocrystals in template-free surfactant hydrothermal environment (Rørvik et al., 2008). Most recently, single-crystalline $KTa_{0.25}Nb_{0.75}O_3$ (KTN) nanorods with an orthorhombic perovskite structure were synthesized via a polymer-assisted hydrothermal method (Hu et al., 2010), the preferred crystallographic orientation of the nanorods were found to be controllable by using different types of polymers in the process; that is, [001]-oriented KTN were obtained upon the use of PVA and [110]-oriented ones were formed with the use of a combination of PAA and PVA. These NWs were produced by controlling the growth condition, and allowed for some initial insights into polarization behavior.

In this chapter, we describe the synthesis of perovskite oxide nanowires/nanorods, such as $(K,Na)NbO_3$ and $Bi_4Ti_3O_{12}$ nanowires/nanorods by hydrothermal process at low temperature (Wang et al., 2010 and Hu et al., 2009). $K_xNa_{1-x}NbO_3$ (with x=0.5) NWs and $(Bi_{3.15}Nd_{0.85})Ti_3O_{12}$ nanorods with diameters of 30~120 nm and length reaching up to several micrometers were synthesized by hydrothermal method. By the use of microstructural measurement and spectra method, the growth dirction, optical properties, phonon vibrational behavior were investigated. In addition, the anisotropic growth mechanism of $K_xNa_{1-x}NbO_3$ NWs was also proposed.

2. Strategies for fabricating ferroelectric NWs

Well-defined ferroelectric NWs are believed to represent exciting systems to investigate fundamental issues about phase structure, intrinsic polarization, piezoelectricity and paraelectricity in one dimension. The main strategy to fabricating ferroelectric NWs is solution based method, including solution-phase decomposition, hydrothermal method, solvothermal method, and composite hydroxide mediated approach etc.

2.1 Solution-phase decomposition (Urban et al., 2002 and Puntes et al., 2001)

The synthesis of perovskite oxide NWs is accomplished by solution-phase decomposition of bimetallic alkoxide precursor in the presence of coordinating ligands, produces the correct product stoichiometry and avoids high-temperature treatment steps, which is similar to the method used to prepare inorganic nanocrystals and nanorods. Figure 1 shows a schematic illustration of typical solution-phase decomposition. It should be noted that rapid injection of organometallic reagents in a hot coordination solvent produces temporally discrete homogeneous nucleation. The decomposition and nucleation occurs rapidly upon injection. The lifetime of monomers in solution is short, and many small metal clusters form simultaneously.

Anisotropic nanorod growth is most likely due to precursor decomposition and crystallization in a structured inverse micelle medium formed by precursors and oleic acid under these reaction conditions. Well-isolated perovskite ferroelectric nanowires can be obtained by sonication of the reaction product followed by fractionation between water and hexane.

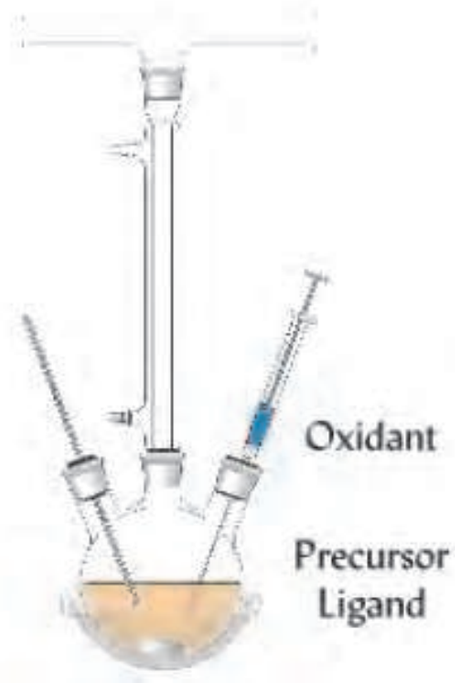

Fig. 1. A schematic illustration of a typical solution-phase decomposition (taken from reference 4).

2.2 Hydrothermal method (Vayssieres et al., 2001)

Hydrothermal method can be defined as a synthesis process of crystals which depends on the solubility of minerals in hot water under high pressure. The crystal growth is performed in an apparatus consisting of a steel pressure vessel called autoclave [Figure 2], in which a nutrient is supplied along with water. As an environmentally benigh reaction medium, the hydrothermal method attracts much attention, which is a promise way for fabricating complex oxide nanomaterials because it can realize a low processing temperature of 200 ^{o}C or less, and can obtain products with high purity. In a typical hydrothermal method, the solubility of a solid is increased in a solvent and the reaction between the solids is sped up under pressures and temperatures above the critical point. A temperature gradient between the opposite ends of the autoclave cause the nutrients dissolve at the hotter end and seeds grow in the cooler end. Possible advantages of the hydrothermal method over other types of crystal growth include the ability to create crystalline phases which are not stable at the melting point, relatively low growth temperatures, and large area production at a low cost. Since most materials can be made soluble in a proper solvent by heating and pressurizing the system close to its critical point. Recently, a new synthetic method based hydrothermal method is used for depositing metal titanate nanowires, such as $BaTiO_3$, $PbTiO_3$ etc (Im et al., 2010). First, a TiO_2 particle thin film is prepared by spray coating, and then transformed to single crystalline titanate nanowires grown on the conducting glass by hydrothermal treatment using TiO_2 particles as seeds of nanowire growth.

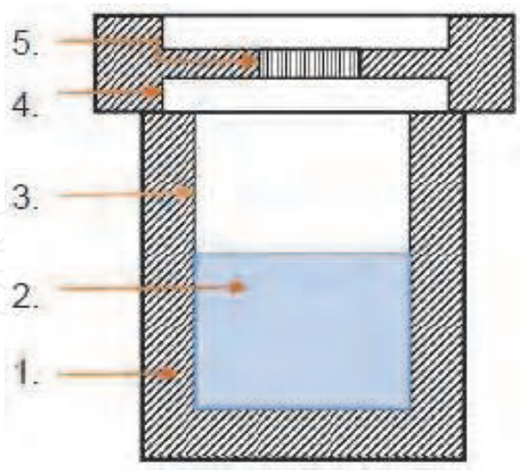

Fig. 2. A schematic illustration of a typical autoclave used in hydrothermal method, which is consist of (1) stainless steel autoclave (2) precursor solution (3) Teflon liner (4) stainless steel lid and (5) spring.

2.3 Solvothermal method

The solvothermal route is similar to the hydrothermal method where the synthesis is also conducted in stainless steel autoclave with the only difference is that the precursor solution is non-aqueous (eg. organic reagents). Heath and co-workers pioneered the use of solvothermal method to synthesize semiconductor nanorods (Heath & Legoues, 1993). The solvothermal method were then employed by many research groups to synthesize all sorts of nanostructures, including metal, semiconductor (Xie & Shang, 2007), graphene (Choucair et al., 2009) and complex oxide nanomaterials (Mao et al., 2005).

The shape, size, morphology and the crystallinity of nanowires can easily be altered through changing certain experimental parameters such as reaction temperature, reaction time, solvent type, surfactant type, and precursor type during a solvothermal system. However, the yield of the final products is very low, and the uniformity in size and morphology is also very poor although solution phase methods seem to be versatile in generating 1D nanostructures.

2.4 Composite hydroxide mediated approach (Liu et al., 2006 and Hu et al., 2009)

The composite-hydroxide-mediated (CHM) approach is based on the use of molten composite hydroxides (KOH and NaOH) as a solvent in chemical reactions at about 200 °C or even less for the synthesis of a wide range of nanostructures. The mixed hydroxides are used to not only mediate the reaction between the raw materials containing cations but also to lower the reaction temperature. Normally, the synthesis process of the CHM method is a one-step process. All of the raw materials with a certain amount of mixed hydroxides are placed within the Teflon vessel at one time. Then, the nanostructures form within the vessel after heating in a furnace at a temperature of ca. 200°C for several hours or days. The environmental appeal of this method arises from its intrinsic scalability,

generality, and facility as well as its fundamental basis on the use of hydroxides as the reaction medium.

3. $(K_{1-x}Na_x)NbO_3$ ferroelectric nanowires (NWs)

Nowadays, piezoelectric materials have been widely used in science and engineering, such as aerospace and medical treatments. Recently, under the requisition of the miniaturization and intergration of devices, low-dimensional piezo- & ferroelectric nanomaterials (nanowires, nanorods and nanotubes, etc.) have attracted much attention because of their potential application in nanodevices such as nanosensors and actuators, nanogenerators and nanopiezotronics (Wang et al., 2006, 2007 and Lao et al., 2007). Alkaline niobates with a perovskite structure, as a promising lead-free piezoelectric and optical material, show excellent piezoelectric, ferroelectric and electro-mechanic properties as well as good nonlinear optical and electro-optical properties (Guo et al., 2003, Saito et al., 2004 and Blomqvist et al., 2003). Potassium sodium niobate [$(K_{1-x}Na_x)NbO_3$, KNN] combines ferroelectrics $KNbO_3$ and anti-ferroelectrics $NaNbO_3$, and have the best piezoelectric properties near the morphology phase boundary (MPB) when x=0.5 in KNN ceramics (Jaeger and Egerton, 1962). However, most reports concerning about KNN materials have concentrated on KNN/KNN-based ceramics rather than KNN nanomaterials. For example, a number of methods have been developed to obtain KNN nano/micro-powders, such as solid-state route, chemical co-precipitation, sol-gel routine, micro-emulsion mediated route and molten-salt process (Villegas et al., 1999, Ravindranathan et al., 1991 and Hayashi et al., 2005). Sun *et al.* synthesized the KNN materials with x = 0.01, 0.24, 0.89, 0.91, 0.99 by a hydrothermal method, but where x has a big jump from 0.24 to 0.89 in composition (Sun et al., 2009). Zhang *et al.* reported the thermodynamic evaluation of KNN material and the hydrothermal preparation (Zhang et al., 2008). So far, the synthesis, electrical or optical properties of low-dimensional KNN nanomaterials such as nanowires and nanorods has been lacking.

3.1 Phase and microstructure of KNN NWs

KNN nanomaterials were synthesized by hydrothermal route using KOH, NaOH and Nb_2O_5 as raw materials. There is a linear relation between the molar ratio of raw material KOH/NaOH and the atomic ratio of K/Na in the final compound, as shown in Figure 3.

Figure 4a shows the XRD patterns of the KNN samples. Sample A to C exhibit single-phase perovskite structure with orthorhombic symmetry (space group: *Amm2*), which can be indexed according to JCPDS card No. 32 - 0822. Moreover, the diffraction peaks of $K_{0.34}Na_{0.66}NbO_3$ (E) can be indexed to single-phase monoclinic perovskite structure with symmetry of space group *Pm*(6), according to the JCPDS card No. 74 - 2024. However, $K_{0.50}Na_{0.50}NbO_3$ (D) shows a main phase of orthorhombic perovskite structure as well as very weak peaks of monoclinic phases which are marked by a black dot in Figure 4a. The phase changes can be clearly proved by the symmetry changes of the (311) and (022) peaks at around 2θ = 56 - 57° (Figure 4b). The lattice parameters of the as-synthesized samples (calculated by MDI JADE5) and crystal structures are listed in Table 1 as well.

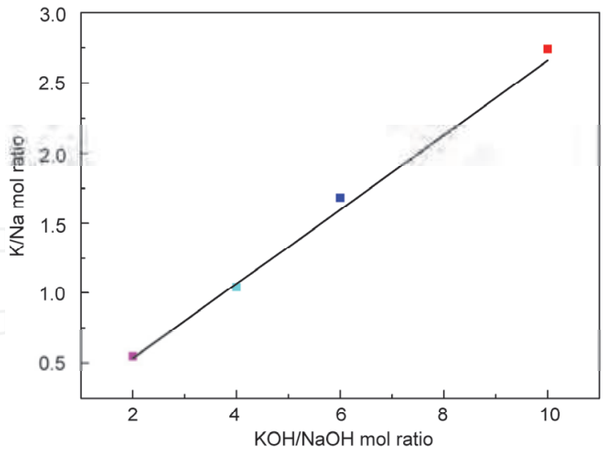

Fig. 3. The relation of molar ratio between the KOH/NaOH of the raw material and K/Na of the samples

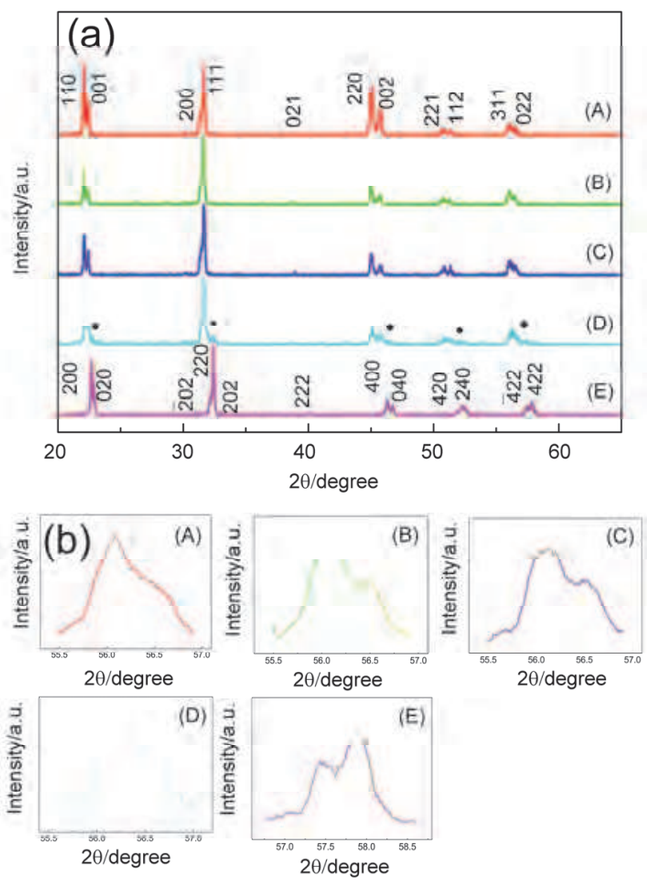

Fig. 4. (a) The XRD patterns in the *2θ* range of 20° to 65° of the as-synthesized $K_{1-x}Na_xNbO_3$ materials with different compositions; (b) The enlarged XRD patterns in the 2θ range of 55° to 58°, which suggest the phase transition by the symmetry changes of the diffraction peaks.

Sample	K/Na/Nb ratio[1]	Syngony	Lattice Parameters			
			a(Å)	*b*(Å)	*c*(Å)	(Å)
A	0.74:0.27:1	Orthorhombic	5.7075(3)	5.6845(4)	3.9689(2)	—
B	0.67:0.34:1	Orthorhombic	5.6837(7)	5.7091(3)	3.9692(0)	—
C	0.64:0.38:1	Orthorhombic	5.6846(5)	5.7039(5)	3.9649(3)	—
D	0.50:0.50:1	Orthorhombic+ Monoclinic	5.6873(8)	5.7041(9)	3.9777(6) [2]	—
E	0.34:0.66:1	Monoclinic	7.8451(1)	7.7719(4)	7.8439(2)	90.558

Table 1. The composition, crystalline phases and lattice parameters of the $K_{1-x}Na_xNbO_3$.

Figure 5 shows the FESEM images of the $K_{0.50}Na_{0.50}NbO_3$ (D) nanowires microstructures synthesized by a hydrothermal process under 200 °C for 24 h. The morphologies are composed of two different structures which are step-like micro-scale particles (Figure 5a) and the intersectional structures of several nanorods/nanofingers (Figure 5b) of 3-5 μm in length and 300-400 nm in width. In order to characterize the detailed microstruture of the products, a single nanorod is separated from the particles shown in Figure 5b. As shown in Figure 6a, the nanowire is about 180 nm in width. The SAED pattern of the nanorod shows clear characteristic diffraction spots of crystalline $K_{0.50}Na_{0.50}NbO_3$, confirming that the nanorod is single-crystalline. In addition, the HRTEM (Figure 4c) show that the interplanar spacings are 3.89 and 3.98 Å, corresponding to the (020) and (002) crystal planes of monoclinic system, respectively. This proves that the monoclinic peaks in curve D of Figure 4a should be the XRD patterns of the nanowires. The results also confirm that the <010> direction is the preferred growth direction of this $K_{0.50}Na_{0.50}NbO_3$ nanorod. Figure 7 shows the microstructure characterization of a single nanofinger taken from the particles shown in Figure 5b. The SAED pattern in Figure 7b also confirmed the single crystalline nature of the nanofinger.

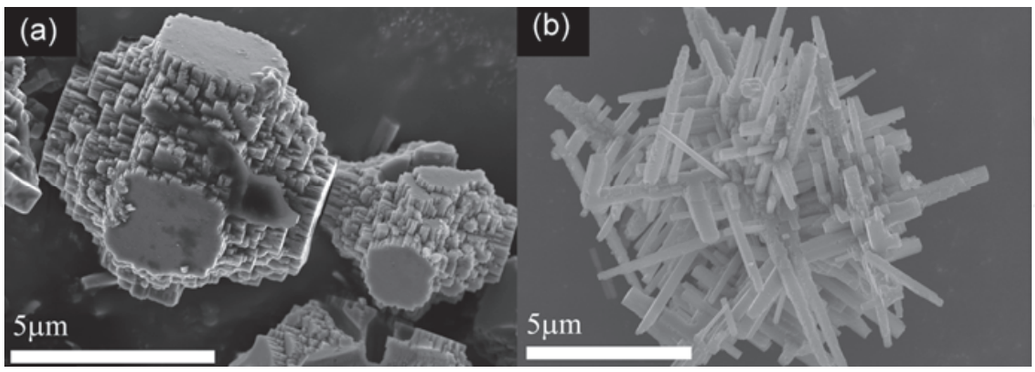

Fig. 5. FESEM images of $K_{0.50}Na_{0.50}NbO_3$ step-like microstructures (a) and nanorods (b).

[1] The K/Na/Nb mol ratios were calculated from XRF results.
[2] The lattice parameters of sample D were calculated according to the diffraction peaks of the orthorhombic phase.

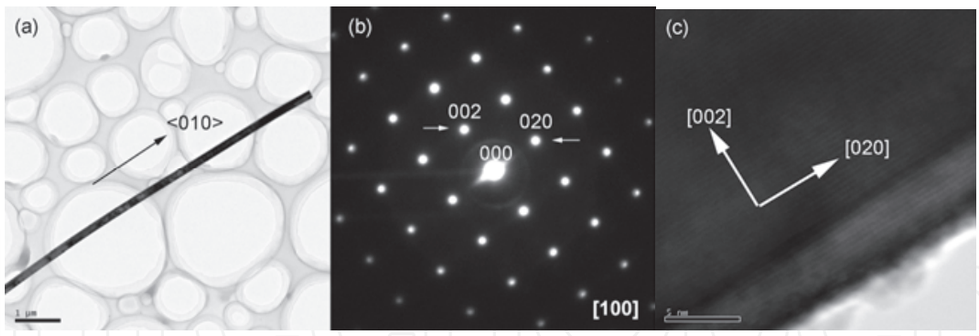

Fig. 6. The TEM results of a single $K_{0.50}Na_{0.50}NbO_3$ nanorod. (a) TEM image; (b) SAED patterns; (c) HRTEM image.

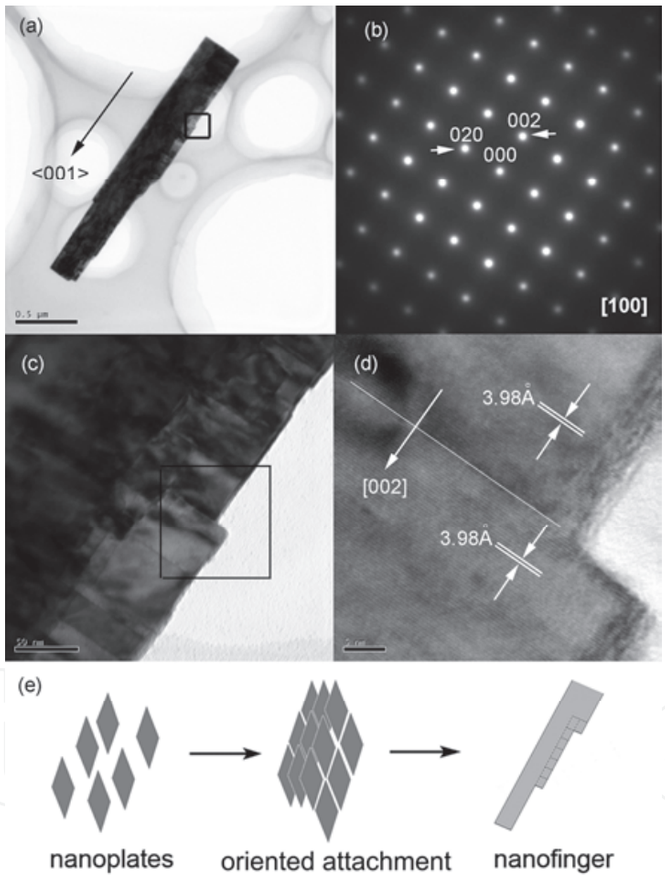

Fig. 7. The TEM results and the formation mechanism of a single $K_{0.50}Na_{0.50}NbO_3$ nanofinger. (a) TEM image; (b) SAED patterns; (c) magnified image of the marked area in (a); (d) HRTEM image of the marked area in (c).

As shown in Figure 7c, the contrast changes at the edge of the nanofinger indicated that it was composed of several nanoplates, which should possess high surface energy and could aggregate easily at the early stage of the hydrothermal process. As shown in Figure 7d, the lattice planes of the two adjacent nanoplates are both (002) with the interplanar spacing of 3.98 Å. Therefore, it is reasonable that the formation of the nanofinger is due to

the oriented attachment growth of the small nanoplates, as illustrated in Figure 7e. The $K_{0.50}Na_{0.50}NbO_3$ nanofinger preferentially grows along <001> direction. Similar results were also found in the hydrothermal fabrication of $KTa_{1-x}Nb_xO_3$ tower-like nanostructure (Hu et al., 2008).

3.2 Optical properties of KNN NWs

Raman scattering properties of the KNN nanomaterials measured at room temperature are shown in Figure 8. According to the XRD results, the structures of sample A to and D belong to the space group C_{2v}^{14} (*Amm2*), which has 12 optical modes in the C_{2v} point group including $4A_1+4B_1+3B_2+A_2$. Among them, all the 12 modes are Raman active and also infrared IR active except the A_2 mode. As shown for spectra A to D, a sharp band shows up on the low-frequency position of 192 cm^{-1}. It was reported that the band at 192 cm^{-1} belongs to a mixed mode of A_1, B_1 and B_2 (Shen et al., 1995). Moreover, there are three bands appeared at 261, 272 and 289 cm^{-1}, which overlap with each other and belong to the vibration mode of B_1(TO), A_1(TO) and A_1(LO)+A_1(TO), respectively. Another three Raman bands show up at the range of 300 – 800 cm^{-1}, including band 430 cm^{-1} of mode A_1(LO), 537 cm^{-1} of mode B_1(TO) and 600 cm^{-1} of mode A_1(TO). In addition, another peak can be observed at 839 cm^{-1}, which belongs to the mode of A_1 (LO). Moreover, 11 Raman bands were observed in spectra E in the range of 150 to 1000 cm^{-1}, which is similar to the Raman spectra of the monoclinic $NaNbO_3$ reported by Chang et al. (Chang et al., 2009).

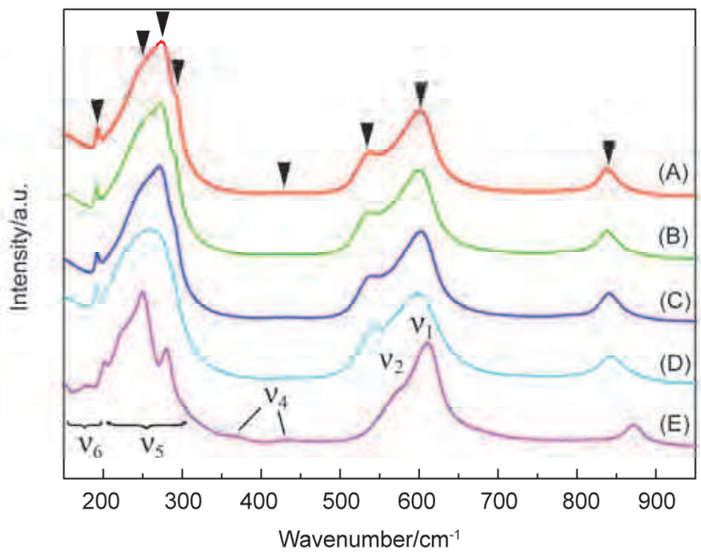

Fig. 8. The room-temperature Raman scattering spectra of the as-synthesized $K_{1-x}Na_xNbO_3$ with different compositions derived from a hydrothermal method.

As reported, the vibration modes of $NaNbO_3$ can be classified as internal modes of the octahedron NbO_6^{7-} anion by the model proposed by Ross (Ross et al., 1970). The vibration modes of the octahedron NbO_6^{7-} anion can be decomposed into two bond stretching vibrations of $A_{1g}(v_1)$ and $E_g(v_2)$, two interbond angle bending vibrations v_5 and v_6 of

symmetry of F_{2g} and F_{2u}, respectively, as well as two vibrations v_3 and v_4 of both F_{1u} symmetry. The vibration modes of $K_{0.34}Na_{0.66}NbO_3$ can be attributed to this explanation as well. Therefore, all Raman bands observed in spectra E can be attributed to the internal modes of octahedron NbO_6^{7-} anion, as shown in Figure 8.

Sample A			Sample E		
Freq./ (cm^{-1})	Assign	$KNbO_3$/ (cm^{-1})	Freq. (cm^{-1})	Assign.	$NaNbO_3$ (cm^{-1})
192	Mixed	196	151		153
261	B_1(TO)	266	177	v_6	175
272	A_1(TO)	280	200		201
289	A_1(LO)+A_1(TO)	298	224		218
430	A_1(LO)	435	248	v_5	247
537	B_1(TO)	535	280		276
600	A_1(TO)	597	368	v_4	378
839	A_1(LO)	836	431		435
			572	v_2	557
			611	v_1	602
			872	v_1+ v_5	867

Table 2. Observed Raman bands and tentative assignments at room temperature.

The band position and corresponding assignment were also listed in Table 2, as well as that of $KNbO_3$ and $NaNbO_3$ (Shen et al., 1998). The transition between orthorhombic (A to D) and monoclinic (E) phase can be clearly confirmed, which is consistent with the XRD results. In addition, as shown in Figure 8 and Table 2, the lower frequency phonon modes shifted downwards from $KNbO_3$ in Ref. 28 to Sample A, while their high frequency phonon modes (535, 597 and 836 cm^{-1}) shifted upwards. Similar phenomenon have also been observed in (Ba,Sr)TiO_3 materials. Because of the different ion radius, ionicity and mass of Na^+ (Sr^{2+}) from K^+ (Ba^{2+}), the introducing of Na^+ (Sr^{2+}) cations to the lattice of $KNbO_3$ ($BaTiO_3$) leads into a perturbation to the original energy levels, which causes a decrease of energy to optical phonons with lower energy and a increase of energy to optical phonons of higher energy, and finally leads to the redshift and blueshift of the low frequency and high frequency phonons, respectively. It can also be explained as a result of a dual function of lattice distortion and mass effect caused by the introducing of Na^+ (Sr^{2+}) (Katiyar et al., 2004). Moreover, 4 bands shifted to high frequency from $K_{0.34}Na_{0.66}NbO_3$ to $NaNbO_3$, while others shifted downwards. It is worth noting that the blueshifted Raman band at 151, 200, 368 cm^{-1} did not appear in the spectra of Sample A, together with the nearly disappeared Raman band at 430 cm^{-1}. It was reported the disappearance of these Raman band in the $KNbO_3$ Raman spectrum could be due to the vanishing of the tilting between the adjacent NbO_6 octahedra. The NbO_6 octahedra in an ideal ABO_3 perovskite structure would be regular with the A site cations surrounded by 12 oxygens and Nb by 6 oxygens. However, such an ideal structure does not exist in the $ANbO_3$ (A = Na and K) because of the tilting of the NbO_6 octahedra and the displacements of Nb atoms from the center position which is induced by the A site cation (Na or K) and the unbalanced interatomic forces present in the perovskite

structures. These distortion depend on the size of the A cations. K^+ cation with a larger size is coordinated to 12 oxygens, thus free space is unavailable for the NbO_6 octahedra to tilt relative to one another. However, Na^+ cation with a relatively small size is coordinated to less than 12 oxygens, and causes an 18° tilt angle between the adjacent NbO_6 octahedra. In KNN structures, with the increasing of Na content, the NbO_6 octahedra begin to tilt with one another and caused the appearance of the four bands in the Raman spectrum of sample E. The blue shift of these four Raman bands from sample E to $NaNbO_3$ may be due to the disappearance of K^+ cation which may restrain the tilting of the NbO_6 octahedra. For the other Raman bands, the red shift may be due to the increasing of distortion in the ABO_3 perovskite structure which leads to a stretching of the bond distance.

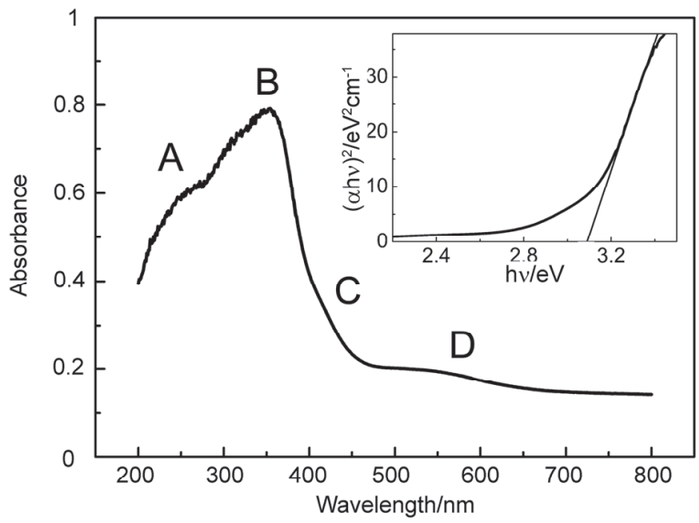

Fig. 9. The UV/Vis absorption spectra of $K_{0.50}Na_{0.50}NbO_3$ synthesized by hydrothermal method. The inset shows the curve obtained through Tauc equation.

Figure 9 shows the UV/Vis absorption spectra of the $K_{0.50}Na_{0.50}NbO_3$ nanowires. As shown, there are four absorption bands appearing at about A (268 nm), B (354 nm), C (411 nm) and D (533 nm). All bands can be found in the spectra of $KNbO_3$, indicate that there is no band attributed to Na^+. According to the results reported by Duan *et al.*, K electron states is shown in the upper part of the conduction band (> 8 eV) and the lower part of the valence band (< -10 eV), indicating that K^+ have no influence to the absorption spectra. According to the calculated density of states (Jehng & Wachs, 1991), band A and B should be attributed to the interband transition from the O_{2p} electron states to the empty Nb_{4d} electron states. Band B originates from a transition from the top of the valence bands occupied by O_{2p} electron states to the bottom of the conduction bands dominated by the empty Nb_{4d} electron states. Band C and D can be attributed to an intraband transition in relation to the Nb^{5+} cations[35]. Furthermore, according to the Tauc equation, the band gaps can be estimated by absorption spectra. The relationship can be illustrated as $(\alpha h\nu)^2 \propto (h\nu - E_g)$ for direct transition, where a and hv is the absorption coefficient and photon energy, respectively. The absorption coefficient a can be defined as $\alpha = \left(2.303 \times 10^3 A\rho\right) / \delta c$, where A, ρ, δ *and* c is the absorbance, theoretical density, sample thickness and the concentration of solution,

respectively. As ρ and *c* are constants and have no relationship with the final result of band gap E_g, the equation can be simplified as $\alpha = 2.303A/\delta$ (δ is estimated to be 0.1 cm for the calculation). The band gap E_g of $K_{0.50}Na_{0.50}NbO_3$ can be obtained by the curve in the inset of Figure 9 to be E_g = 3.09 eV.

3.3 Growth mechanism of KNN NWs

As previously reported, $KNbO_3$ nanostructures were synthesized in solution via a dissolution-precipitation process (Goh et al., 2003). Nb_2O_5 is dissolved into $Nb_6O_{19}^{8-}$ ions, and forms a octahedron of NbO_6^{7-} anions by a complex transformation, which act as elementary species to produce the precipitation of $KNbO_3$ perovskite. Similarly, the mechanism can be applied to the formation of KNN material as well. These reactions are formulated as follows:

$$3Nb_2O_5 + 8OH^- \longrightarrow Nb_6O_{19}^{8-} + 4H_2O \quad (1)$$

$$Nb_6O_{19}^{8-} + 34OH^- \longrightarrow 6NbO_6^{7-} + 17H_2O \quad (2)$$

$$NbO_6^{7-} + (1-x)K^+ + xNa^+ + 3H_2O \longrightarrow K_{1-x}Na_xNbO_3 + 6OH^- \quad (3)$$

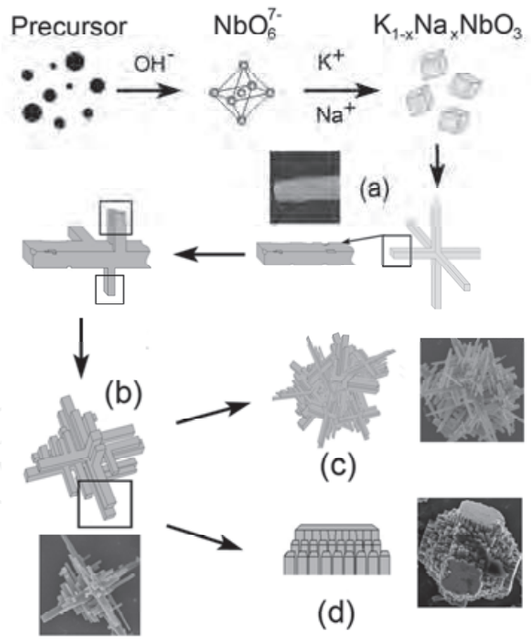

Fig. 10. The schematic illustration of the formation process of $K_{0.50}Na_{0.50}NbO_3$ nano/micro-structures by hydrothermal process.

As described by reaction (1), the Nb_2O_5 was dissolved simultaneously into the $Nb_6O_{19}^{8-}$ ions at the initial stage of the hydrothermal reaction. Then single octahedron NbO_6^{7-} anions were formed by complex transformation occurred under higher alkaline conditions after reaction

(2). Reaction (3) referred to the tiny crystalline nucleation in a supersaturated medium followed by the crystal growth of KNN under hydrothermal conditions. The formation process of the $K_{0.50}Na_{0.50}NbO_3$ nanostructure is illustrated in Figure 10. The reaction happened simultaneously with the crystalline nucleation due to the high supersaturation of medium at the initial stage, which promoted the continuous growth of KNN crystals, and formed several crystalline nucleuses. Once the supersaturation was reduced to a certain extent, polarization growth became a major process.

As shown in Figure 10, the {001} family of crystal planes are the polar faces of the NbO_6^{7-} structure. The dipoles exist along <001> orientation because of the Nb^{5+} and O^{2-} layers arranging alternately along this orientation. The {001} faces are therefore unstable when Nb^{5+} or O^{2-} is exposed. As a result, the crystal growth along <001> orientations are predominant in energy, along which the polarization growth occurred. Several nanorods were formed along these six directions, which formed the cross-like structures. The different growth direction shown in Figure 6a and Figure 7a could prove this supposition. Moreover, the surface of the as-formed nanorods/nanofingers served as the substrate for the latter one. Gradually, more nanorods/nanofingers would grow up while the original one grew longer. According to this tendency, the grain grew larger step by step (Figure 10b), then the grains near each other may grow together, and formed a larger structure that consisted of a number of nanorods interlacing with each other (Figure 10c). As the reaction continued, nanorods which have the same orientation and near each other gradually grew together due to the aggregation growth happened during the hydrothermal reaction process, and formed step-like particles shown in Figure 10d. Therefore, the growth of the as-prepared $K_{0.50}Na_{0.50}NbO_3$ should be due to crystal structure of the octahedron NbO_6^{7-} anions as well as the oriented attachment and the aggregation growth mechanism.

4. $Bi_4Ti_3O_{12}$ (BiT) ferroelectric NRs

To enrich the physics of ferroelectricity, especially at one dimensional nanoscale, perfectly structured polar oxide nanomaterials are the optimal samples for study. Ferroelectric bismuth layered perovskite materials, with the characteristics of fast switching speed, high fatigue resistance and good retention (Araujo et al., 1995), are currently studied extensively due to their potential in several important areas, including nonvolatile random access memories (Nv-FRAM), room temperature pyroelectric devices, electro-optic devices, and microelectro-mechanical systems etc (Scott, 1998). Among these bismuth layered ferroelectric oxides, lanthanide-modified bismuth titanate ($Bi_{4-x}R_xTi_3O_{12}$, R=La, Nd, Sm, etc.), especially for $Bi_{4-x}Nd_xTi_3O_{12}$, are regarded as one of the very important candidate for the Nv-FRAM applications because of its excellent ferroelectric properties, e.g., much improved fatigue resistance, larger remanent polarization, lead-free nature and relatively lower processing temperature in comparison to $Pb(Zr,Ti)O_3$ (PZT) and $SrBi_2Ta_2O_9$ (SBT) (Park et al., 1999 and Lee et al., 2006). Despite the extensive studies of $Bi_{4-x}Nd_xTi_3O_{12}$, however, most of these were focused on ceramics and thin films; a clear fundamental study of such low-dimensional (nanowires or nanorods) ferroelectric nanostructure has been lacking, including the phase transformation, domain structures and optical properties induced by their reduced dimensionality etc.

4.1 Phase and microstructure of BiT NRs

The BNT nanorods were fabricated by hydrothermal method using bismuth nitrate pentahydrate, $Bi(NO_3)_3 \cdot 5H_2O$, neodymium nitrate hexahydrate, $Nd(NO_3)_3 \cdot 6H_2O$, tetrabutyl titanate, $Ti(OC_4H_9)_4$ as the starting materials, NaOH served as a mineralizer and polyvinyl alcohol (PVA-124) as the additive.

Figure 11a shows the XRD pattern of BNT nanorods sample derived from hydrothermal method. As shown, all of the diffraction peaks can be indexed as the orthorhombic structure of $Bi_{3.15}Nd_{0.85}Ti_3O_{12}$ powders with the lattice constants: a=5.4526Å, b=5.4242Å, c=32.0249Å, agreement well with the standard literature value (JCPDS Card NO.36-1486, a=5.429, b=5.405 and c=32.83 Å), which exhibits that the products are composed of BNT with perovskite structure and without the trace of any impurity phase. Figure 11b shows the typical FESEM images of the BNT nanorods dispersed on the silicon substrate. It can be seen that a majority of the nanorods grow into regular structure and almost all of the nanorods have smooth surface and uniform dimension. The diameters of nanorods are range of 30~120 nm and length reaching up to several micrometers, which are promising candidate for nanoscale ferroelectric sensors. In addition, it is worth noting that larger amount of small particles with unregular morphologies absorbing on the surface of BNT nanorods, which may be the PVA amorphous phase.

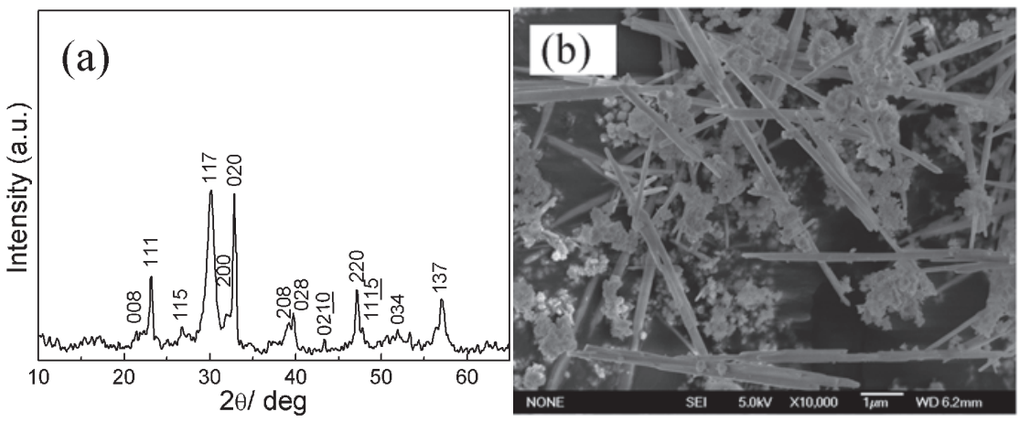

Fig. 11. (a) X-ray diffraction pattern of the as-prepared products composed of randomly oriented BNT nanorods together with small amount of particles. (b) Field emission SEM images of the BNT nanorods.

Figure 12 shows the TEM, HRTEM image, energy-dispersive X-ray analysis (EDS, inset in Figure2a) and SAED pattern (inset in Figure 12c) of BNT single nanorods. As exhibited in Figure 12a and 2b, the as-synthesized nanorods have diameters of 30~120 nm and with smooth surface and uniform cross section along their length. And EDS shows the presence of Bi, Ti, Nd and O. The HRTEM image in Figure 12c shows the clear lattice fringes, which indicates the BNT nanorods are structurally uniform with well crystallized. The adjacent lattice spacing is 0.325 nm, which corresponds to the (00$\underline{1}$0) crystal planes, confirming that [104] is the preferred growth direction of the BNT nanorods. The SAED pattern shows clear diffraction spots characteristic of crystalline BNT, which confirm the single-crystalline nature of these nanorods. The SAED pattern shows clear diffraction spots characteristic of crystalline BNT obtained from the region of single nanorod, which suggests that the BNT nanorod has orthorhombic structure and single-crystalline in nature.

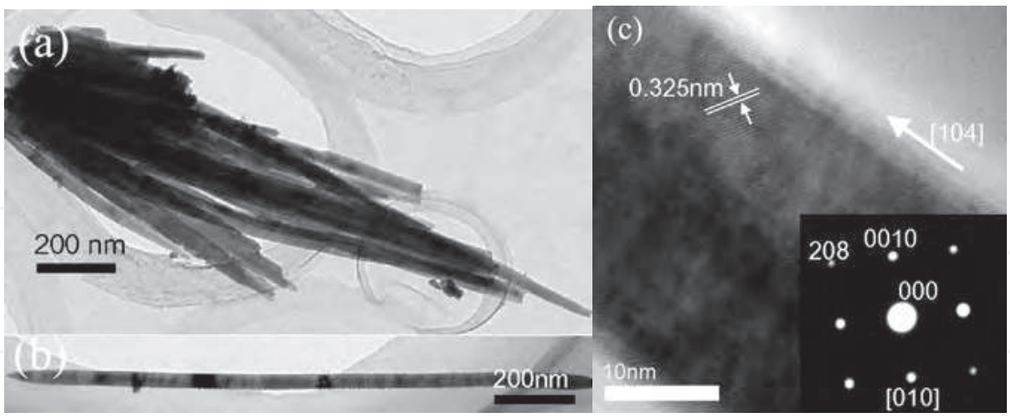

Fig. 12. (a) TEM image of the BNT nanorods; the inset is EDS spectrum of nanorods showing four elements of Bi, Ti, Nd and O. (b) The TEM image of individual BNT nanorod. (c) The HRTEM image of a single-crystal BNT nanorod and its corresponding SAED pattern (inset).

4.2 Raman spectroscopy of BiT NRs

Figure 13 illustrates the Raman spectra obtained from the BNT nanorods, with a spectrum from BIT powders for comparison. One can see that ten Raman active modes (indicated by black arrows) were observed for orthorhombic phase BNT nanorods. The number of modes cannot fulfill the selection rule, which may be due to the broken symmetry, mode overdamping, and mode overlapping, making some modes unidentified (Yau et al., 2004).

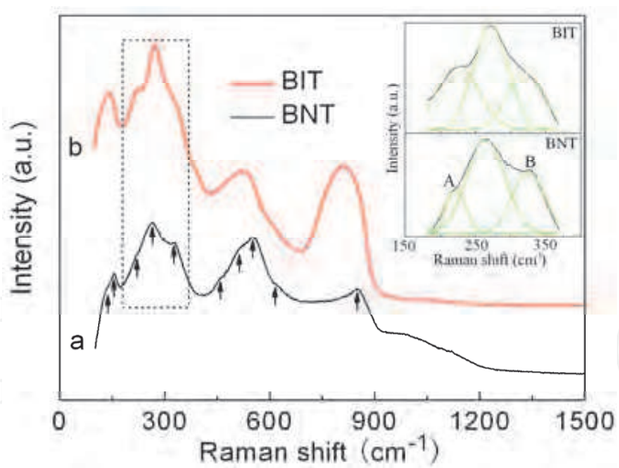

Fig. 13. Raman scattering spectrum of the BNT nanorods with the comparison of BIT samples was measured at room temperature at an excitation wavelength of 514.5 nm. The inset shows the comparison of three peaks prominently at about 220, 265 and 320 cm^{-1} between BNT nanorods and BIT samples, the solid line is the original experimental data and the dashed lines are the Gaussian fitted curves.

Comparing with the Raman spectrum of BIT powders, most modes of the BNT nanorods are overdamped and highly shifted. The splitting of the mode at about 550 cm^{-1} (B_{2g}/B_{3g}) in BIT powders into two well-defined modes (510 and 552 cm^{-1}) in BNT nanorods suggests a

symmetry breaking effect. It has been reported that Raman modes from about 121.6 cm^{-1} to the one above 600 cm^{-1} of BIT films were all corresponding to the vibrations inside the perovskite-like slab (Yao et al., 2004). In our case, the first two modes at about 130 and 155 cm^{-1} for BNT nanorods could be assigned to the outer vibration modes between Bi atoms and octahedron, which are upshifted and with a decrease in intensities compare to BIT. A mode at about 220 cm^{-1} (B_{2g}+B_{3g}) is due to the x(y) axis vibration of oxygen atoms, which is highly overdamped with Nd incorporated into the A site of the perovskite slab compared to that of BIT powders. The internal mode at about 265 cm^{-1} (B_{2g}+B_{3g}) is for internal angle bending vibration; the one at 320 cm^{-1} (A_{1g}) is for a combination of stretching and bending according to the literature (Kojima et al., 1994). The Gaussian fitted Raman spectra [dashed line inset of Figure 13] of the most intensive peaks in the Raman spectra gives the differences between BNT nanorods and BIT powders. Comparing to the Raman modes of BIT powders, the intensity of the shoulder peak of lower frequency (denoted by "A") decreased and the higher (denoted by "B") increased, and the full width at half maximum of these two peaks decreased as Nd doped in BIT, which may be due to the stretching of the Ti-O bonds in x(y) lattice plane according to the XRD results. In addition, the mode at about 552 cm^{-1} with its shoulder (510 cm^{-1}) and 850 cm^{-1} (A_{1g}) of BNT are corresponding to the distortion of the TiO_6 octahedron of perovskite unit $(Bi_2Ti_3O_{10})^{2-}$ slab (Yao et al., 2004). The internal mode at about 615 cm^{-1} could derive from the stretching of the O-Ti-O-Ti-O-Ti-O octahedral chain between two Bi_2O_2 layers. Nevertheless, the Raman intensity of the 850 cm^{-1} mode is lower than that of BIT, which indicates that the internal vibration of TiO_6 octahedrons decrease as Nd doped into BIT.

4.3 XPS analysis of BiT NRs

Figure 14 show the narrow scan XPS spectra of BNT nanorods. It can be seen clearly that the nanorods are consisted of four elements Bi, Ti, Nd, and O, which are agreeing with the EDS results. Figure 14a is the photoemission spectrum of Bi4*f* core level peak, which show two sets of spin-orbit doublet components peaking at about 158.5 and 163.8 eV, with a typical Bi4*f* spin-orbit splitting of 5.3 eV closed to the value of 5.4 eV for BIT samples, and 5.3 eV for $Bi_{4-x}La_xTi_3O_{12}$ (BLT) (Jovalekic et al., 1998 and Chu et al., 2002). In addition, the spin-orbit doublet with weak intensities emerge in the spectrum overlapping with the major Bi4*f* photoemission at the high BE side fitted by Gaussian function. The peak positions of lower BE components located at 155.8 and 160.5 eV, show a chemical shift of 2.7 and 3.3 eV with respect to the main peaks, respectively. These are consistent with the typical value of 3.0±0.1 eV between Bi^0 and Bi_2O_3 (Kim et al., 2003), indicated the possibility appearance of Bi^{+3-x} at the surface of BNT nanorods with only several monolayers, which may be due to a deficiency in oxygen and an enhanced concentration of oxygen vacancies in the vicinity of bismuth cations, either in the perovskite lattice structure or in the Bi_2O_2 layer (Jovalekic et al., 1998). The XPS narrow scan spectrum of Bi4*d* and Ti2*p* core level is shown in Figure 14b. For BNT nanorods, the Ti2$p_{3/2}$ photoelectron peak occurred in the XPS spectrum as a distinctively resolved feature located at a BE position of about 457.8 eV, which is lower than the BLT of 461.38 eV, but is very closed to the $PbTiO_3$ ceramics of 457.9 eV (Kim et al., 2003). This indicates the 4+ valence state of the titanium atoms within the perovskite layer of bismuth titanate, which supports our assumption about the oxygen vacancies residing inside the Bi_2O_2 layer. The Ti2$p_{1/2}$ photoemission is overlapped by the Bi4$d_{3/2}$ core level peak located at 465.1 and 465.2 eV respectively. The spin-orbit splitting of Ti2*p* is 7.3 eV larger than the corresponding value of 5.7

eV for BLT (Chu et al., 2002), which may be due to the lattice shrinking derived from the size-effect of BNT nanorods. Figure 14c exhibits the photoemission spectrum of Nd4*d* core level peak. Only one component located at 121 eV was detected for BNT nanorods, suggests Nd-O bond is stable in the crystal. Figure 14d shows the XPS narrow scan spectrum of O1*s* core level peak. The lineshape of the O1*s* photoemission reveals three peaks fitted by Gaussian-based function. It has been reported that the oxygen atom in a stronger Ti–O bond carries a higher effective negative charge than in a weaker Bi–O bond. Hence, the first one located at 529.7 eV was assigned to the lattice oxygen of Ti-O bonds in the BNT nanorods, while the second one located at 532 eV was assigned to the oxygen of Bi-O bonds. The third one located at 533.5 eV could be ascribed to OH groups likely to be present on the surface of the grains, which are very common in samples with high surface energy.

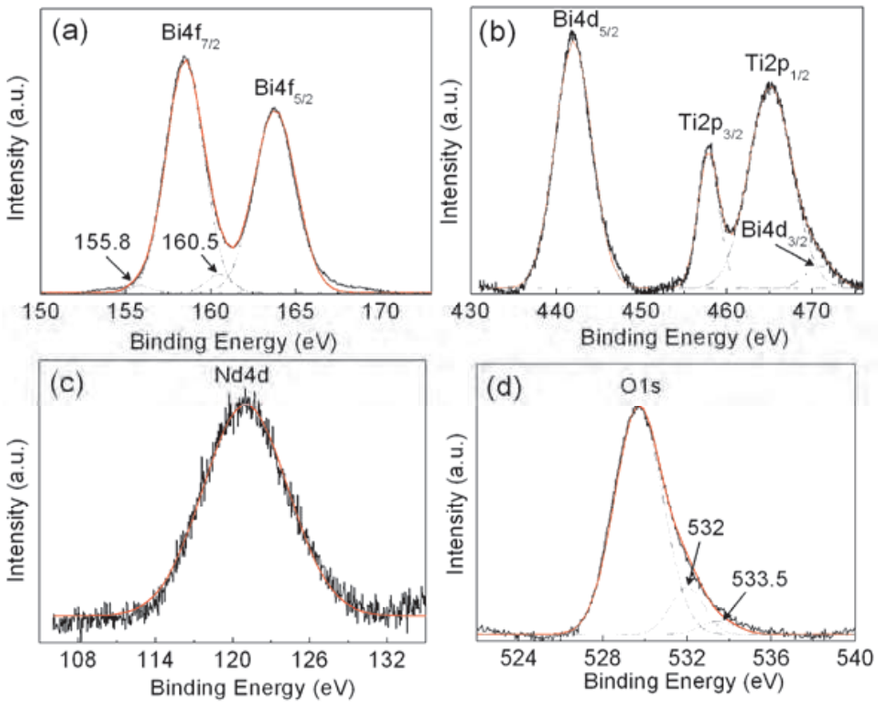

Fig. 14. Core level photoemission spectra of BNT nanorods: (a) Bi4*f*; (b) Bi4*d* and Ti2*p*; (c) Nd4*d*; (d) O1*s*, respectively.

5. Conclusion

1-D perovskite ferroelectric nanomaterials of (K,Na)NbO_3 and $Bi_4Ti_3O_{12}$ nanowires/ nanorods with certain orientations were synthesized by hydrothermal approach. The anisotropic growth of (K,Na)NbO_3 nanowires was dependent on its tetragonal structures, while it's not the case for the growth of 1-D $Bi_4Ti_3O_{12}$ nanomaterials, which should be determined by the difference of surface energy derived from the existence of surfactants. The (K,Na)NbO_3 nanorods were composed of larger amounts of nanoplates with the same orientation, which indicated that the nanorods formed due to the oriented attachment growth. Moreover, the formation of the step-like particles should be due to the aggregation growth. The polarization, piezoelectricity and mechanical-electric properties are

forthcoming. These nanowires/ nanorods may be promising candidate for future nanoscale ferroelectric sensors or other functional nanodevices etc.

6. Acknowledgment

Financial support for this work was provided by the National Natural Science Foundation of China (Grant 90923013, 50902046 and 50872031), the Natural Science Fundation of Hubei Province of China (2009CDB085), and International Cooperation Project of Wuhan City (201070934340).

7. References

Araujo, C.A.; Cuhair, J.D.; McMillan, L.D.; et al. (1995). Fatigue-free ferroelectric capacitors with platinum electrodes. *Nature* Vol.374, p. 627-629

Bhalla, A.S.; Guo, R.; Roy, R. (2000). The perovskite structure – a review of its role in ceramic science and technology. *Materials Research Innovations*, Vol.4, No.1, p. 3-26.

Blomqvist, M.; Khartsev, S.; Grishin, A.; et al. (2003). Optical waveguiding in magnetron-sputtered $Na_{0.5}K_{0.5}NbO_3$ thin films on sapphire substrates. *Applied Physics Letters*, Vol.82, No.3, p. 439-441

Choucair, M.; Thordarson, P.; Stride, J.A. (2009). Gram-scale production of graphene based on solvothermal synthesis and sonication. *Nature Nanotechnology* Vol.4, p. 30-33

Chang, Y.F.; Yang, Z.P.; Dong, M.Y.; et al. (2009). Phase structure, morphology, and Raman characteristics of $NaNbO_3$ particles synthesized by different methods. *Materials Research Bulletin*, Vol.44, No.3, p. 538-542

Chu, M.W.; Ganne, M.; Galdes, M.T.; Brohan, L. (2002). X-ray photoelectron spectroscopy and high resolution electron microscopy studies of Aurivillius compounds: $Bi_{4-x}La_xTi_3O_{12}$ (x=0, 0.5, 0.75, 1.0, 1.5, and 2.0). *Journal of Applied Physics*, Vol.91, No.5, p. 3178-3187

Goh, G.K.L.; Lange, F.F; Haile, S.M.; Levi, C.G.J. (2003). Hydrothermal synthesis of $KNbO_3$ and $NaNbO_3$ powders. *Journal of Materials Research*, Vol.18, 338-345

Guo, Y.P.; Luo, H.S.; Ling, D.; et al. (2003). The phase transition sequence and the location of the morphotropic phase boundary region in $(1-x)PbMg_{1/3}Nb_{2/3}O_3$- $xPbTiO_3$ single crystal. *Journal of Physics*: *Condensed Matter*, Vol.15, No.2, p.L77-L82

Hayashi, H.; Hakuta, Y.; Kurata, Y.J. (2005). Hydrothermal synthesis of potassium niobate photocatalysts under subcritical and supercritical water conditions. *Journal of Materials Chemistry*, Vol.14, No.13, p. 2046-2051

Heath, J.R.; Legoues, F.K. (1993). A liquid solution synthesis of single crystal germanium quantum wires. *Chemical Physics Letters*, Vol.208, No.3-4, p. 263-268

Hu, Y.M.; Gu, H.S.; Zhou, D.; et al. (2010). Orientation-Control Synthesis of $KTa_{0.25}Nb_{0.75}O_3$ Nanorods. *Journal of America Ceramic Society*, Vol.93, No.3, p. 609-613

Hu, Y.M.; Gu, H.S.; Hu, Z.L.; et al. (2008). Controllable Hydrothermal Synthesis of $KTa_{1-x}Nb_xO_3$ Nanostructures with Various Morphologies and Their Growth Mechanisms. *Crystal Growth & Design*, Vol.8, No.3, p. 832-837

Hu, C.; Xi, Y.; Liu, H.; Wang, Z.L. (2009). Composite-hydroxide-mediated approach as a general methodology for synthesizing nanostructures. *Journal of Materials Chemistry*, Vol.19, No.7, p. 858-868

Hu, Z.; Gu, H.; Hu, Y.; et al. (2009). Microstructural, Raman and XPS properties of single-crystalline $Bi_{3.15}Nd_{0.85}Ti_3O_{12}$ nanorods. *Materials Chemistry and Physics*, Vol.113, No.1, p. 42-45

Im, B.; Joshi, U.A.; Lee, K.H.; et al. (2010). Growth of single crystalline barium titanate nanowires from TiO_2 seeds deposited on conducting glass. *Nanotechnology*, Vol.21, No.42, p. 425601

Jaeger, R.E.; Egerton, L. (1962). Hot pressing of potassium-sodium niobates. *Journal of American Ceramic Society*, Vol.45, No.5, p. 209-213

Jehng, J.M.; Wachs, I.E. (1991). Structural chemistry and Raman spectra of niobium oxides. *Chemistry of Materials*, Vol.3, No.1, p. 100-107

Jovalekic, C.; Pavlovic, M.; Osmokrovic, P.; Atanasoska, L. (1998). X-ray photoelectron spectroscopy study of $Bi_4Ti_3O_{12}$ ferroelectric ceramics. *Applied Physics Letters*, Vol.72, No.9, p. 1051-1053

Kojima, S.; Imaizumi, R.; Hamazaki, S.; Takashige, M. (1994). Raman scattering study of bismuth layer-structure ferroelectric. *Japanese Journal of Applied Physics*, Vol.33, p. 5559-5564

Katiyar, R.S.; Jain, M.; Yuzyuk, Y.I. (2004). Raman Spectroscopy of Bulk and Thin-Layer (Ba,Sr)TiO_3 Ferroelectrics. *Ferroelectrics*, Vol.303, p. 699-705

Kim, J.N.; Shin, K.S.; Park, B.O.; et al. (2003). Characterization of ferroelectric ceramics using x-ray diffraction, transmission electron microscopy, and x-ray photoelectron spectroscopy. *Smart Materials Structures*, Vol.12, No.4, p. 565-569

Lao, C.S.; Kuang, Q.; Wang, Z.L.; et al. (2007). Polymer functionalized piezoelectric-FET as humidity/ chemical nanosensors. *Applied Physics Letters*, Vol.90, p. 262107

Lee, S.K.; Hesse, D.; Gosele, U. (2006). Growth and properties of (104)-oriented ferroelectric Nd-substituted $Bi_4Ti_3O_{12}$ films on Si (100) using (111)-oriented $SrRuO_3$/Pt electrodes. *Applied Physics Letters*, Vol.88, p. 062909

Liu, H.; Hu, C.; Wang, Z.L. (2006). Composite-Hydroxide-Mediated Approach for the Synthesis of Nanostructures of Complex Functional-Oxides. *Nano Letters*, Vol.6, No.7, p. 1535-1540

Lu, C.H.; Lo, S.Y.; Wang, Y.L. (2002). Glycothermal preparation of potassium niobate ceramics particles under supercritical conditions. *Materials Letters*, Vol.55, No.1-2, p. 121-125

Magrez, A.; Vasco, E.; Seo, J.W.; et al (2006). Growth of Single-Crystalline $KNbO_3$ Nanostructures. *Journal of Physics Chemical B*, Vol.110, No.1, p. 58-61

Mao, Y.; Park, T.J.; Wong, S.S. (2005). Synthesis of classes of ternary metal oxide nanostructures. *Chemistry Communication*, No.46, p. 5721-5735

Park, B.H.; Kang, B.S.; Bu, S.D.; et al. (1999). Lanthanum-substituted bismuth titanate for use in non-volatile memories. *Nature*, Vol.401, p. 682-684

Puntes, V.F.; Krishnan, K.M.; Alivisatos, A.P. (2001). Colloidal Nanocrystal Shape and Size control: The Case of Cobalt. *Science*, Vol.291, p. 2115-2117

Ravindranathan, P.; Komarneni, S.; Bhalla, A.S.; Roy, R. (1991). Synthesis and dielectric properties of solution sol-gel derived $0.9(Mg_{1/3}Nb_{2/3})O_3$-$0.1PbTiO_3$ ceramics. *Journal of American Ceramic Society*, Vol.74, No.12, p. 2996-2999

Ross, S.D. (1970). The vibrational spectra of lithium niobate, barium sodium niobate and barium sodium tantalite. *Journal of Physics C: Solid State Physics*, Vol.3, No.8, p.1785

Rørvik, P.M.; Almli, Å.; Helvoort, A.T.J.; et al. (2008). $PbTiO_3$ nanorod arrays grown by self-assembly of nanocrystals. *Nanotechnology*, Vol.19, No.22, p. 225605 (1-6)

Saito, Y.; Takao, H.; Tani, T.; et al. (2004). Lead-free piezoceramics. Nature, Vol.432, p. 84-87

Scott, J.F. (1998). The physics of ferroelectric ceramic thin films for memory applications. *Ferroelectric Review*, Vol.1, p. 1-30

Shen, Z.X.; Hu, Z.P.; Chong, T.C.; et al. (1995). Pressure-induced strong mode coupling and phase transitions in $KNbO_3$. *Physics Review B,* Vol.52, p. 3976-3980

Shen, Z.X.; Wang, X.B.; Kuok M.H.; Tang, S.H. (1998). Raman scattering investigations of the antiferroelectric-ferroelectric phase transition of $NaNbO_3$. *Journal of Raman Spectroscopy*, Vol.29, No.5, p. 379-384

Spanier, J.E.; Kolpak, A.M.; Urban, J.J.; et al. (2006). Ferroelectric Phase Transition in Individual Single-Crystalline $BaTiO_3$ NWs. *Nano Letters*, Vol.6, No.4, p. 735-739

Sun, X.; Chen, J.; Yu, R. et al. (2009). $BiScO_3$ doped $(Na_{0.5}K_{0.5})NbO_3$ lead-free piezoelectric ceramics. *Journal of American Ceramic Society*, Vol.92, No.1, p. 130-132.

Urban, J.J.; Yun, W.S.; Gu, Q.; and Park H. (2002). Synthesis of Single-Crystalline Perovskite Nanorods Composed of Barium Titanate and Strontium Titanate. *Journal of American Chemistry Society*, Vol.124, No.7, p. 1186-1187

Vayssieres, L.; Keis, K.S.; Lindquist, E.; and Hagfeldt, A. (2001). Purpose-bult anisotropic metal oxide material: 3D highly oriented microrod array of ZnO. *Journal of Physics Chemistry B*, Vol.105, No.17, p. 3350-3352

Villegas, M.; Caballero, A.C.; Moure, C.; et al. (1999). Low-temperature sintering and electrical properties of chemically w-doped $Bi_4Ti_3O_{12}$ ceramics. *Journal of the European Ceramic Society*, Vol.19, No.6-7, p. 1183-1186

Wang, X.D.; Zhou, J.; Song, J.H.; et al. (2006). Piezoelectric field effect transistor and nanoforce sensor based on a single ZnO nanowires. *Nano Letters*, Vol.6, No.12, p. 2768-2772

Wang, X.D.; Song, J.H.; Liu, J.; Wang, Z.L. (2007). Direct-current nanogenerator driven by ultrasonic waves. *Science*, Vol.316, No.5821, p. 102-105

Wang, Z.; Gu, H.; Hu, Y.; et al. (2010). Synthesis, growth mechanism and optical properties of $(K,Na)NbO_3$ nanostructures. *CrystEngComm*, Vol.12, p. 3157-3162

Wei, N.; Zhang, D.M. ; Han, X.Y.; et al. (2007). Synthesis and mechanism of ferroelectric potassium tantalate niobate nanoparticles by the solvothermal and hydrothermal processes. *Journal of American Ceramics Society*, Vol.90, No.5, p. 1434-1437

Xie, R.C.; and Shang, J.K. (2007). Morphological control in solvothermal synthesis of titanium oxide. *Jourla of Material Science* Vol.42, No.16, p. 6583-6589

Xu, G.; Ren, Z.; Du, P.; et al. (2005). Polymer-Assisted Hydrothermal Synthesis of Single-Crystalline Tetragonal Perovskite $PbZr_{0.52}Ti_{0.48}O_3$ NWs. *Advanced Materials*, Vol.17, No.7, p. 907-910

Yau, C.Y.; Palan, R.; Tran, K.; Buchanan, R.C. (2004). Raman study of Bi site-occupancy effect on orientation and polarization in $Bi_4Ti_3O_{12}$ thin films. *Applied Physics* Letters, Vol.85, No.20, p. 4714-4716

Zhang, C.; Lv, H.J.; Guo, M.; et al. (2008). Thermodynamic evaluation and hydrothermal preparation of $K_xNa_{1-x}NbO_3$. *Rare Metals*, Vol.27, No.4, p. 371-377

Nanowires - Fundamental Research

Edited by Dr. Abbass Hashim

ISBN 978-953-307-327-9
Hard cover, 552 pages
Publisher InTech
Published online 19, July, 2011
Published in print edition July, 2011

Understanding and building up the foundation of nanowire concept is a high requirement and a bridge to new technologies. Any attempt in such direction is considered as one step forward in the challenge of advanced nanotechnology. In the last few years, InTech scientific publisher has been taking the initiative of helping worldwide scientists to share and improve the methods and the nanowire technology. This book is one of InTechâ€™s attempts to contribute to the promotion of this technology.

How to reference

In order to correctly reference this scholarly work, feel free to copy and paste the following:

Yongming Hu, Haoshuang Gu and Zhao Wang (2011). The Anisotropic Growth of Perovskite Oxide Nanowires, Nanowires - Fundamental Research, Dr. Abbass Hashim (Ed.), ISBN: 978-953-307-327-9, InTech, Available from: http://www.intechopen.com/books/nanowires-fundamental-research/the-anisotropic-growth-of-perovskite-oxide-nanowires

INTECH
open science | open minds

InTech Europe
University Campus STeP Ri
Slavka Krautzeka 83/A
51000 Rijeka, Croatia
Phone: +385 (51) 770 447
Fax: +385 (51) 686 166
www.intechopen.com

InTech China
Unit 405, Office Block, Hotel Equatorial Shanghai
No.65, Yan An Road (West), Shanghai, 200040, China
中国上海市延安西路65号上海国际贵都大饭店办公楼405单元
Phone: +86-21-62489820
Fax: +86-21-62489821

IntechOpen